Robotica (2010) volume 28, pp. 621–635. © Cambridge University Press 2009
doi:10.1017/S0263574709990373

# A manoeuvre control strategy for flexible-joint manipulators with joint dry friction

H. Salmasi, R. Fotouhi* and P. N. Nikiforuk

*Mechanical Engineering Department, University of Saskatchewan, 57 Campus Drive, Saskatoon, Canada S7N 5A9*

(Received in Final Form: July 23, 2009. First published online: August 27, 2009)

**SUMMARY**

A new control strategy based on the singular perturbation method and integral manifold concept is introduced for flexible-joint manipulators with joint friction. In controllers so far developed based on the singular perturbation theory, the dynamics of actuators of flexible-joint manipulators are partially modelled, and the coupling between actuators and links is ignored. This assumption leads to inaccuracy in control performance and error in trajectory tracking which is crucial in high-precision manipulation tasks. In this paper, a comprehensive dynamic model which takes into account the coupling between actuators and links is developed and a composite controller is then designed based on the singular perturbation theorem and integral manifold concept. To overcome the joint friction, a novel method is introduced in which a linear feed-forward torque is designed using the principle of work and energy. Finally, the experimental set-up of a single rigid-link flexible-joint manipulator in the Robotics Laboratory at the University of Saskatchewan is used to verify the proposed controller. Experimental results employing the new controller show that the trajectory tracking error during and at the end of the motion of the robot manipulator is significantly reduced.

KEYWORDS: Flexible-joint manipulator; Dry friction; Integral manifold controller.

## 1. Introduction

A wide variety of robots is now employed in different areas such as spacecraft and vehicle manufacturing. In most of these robot manipulators, a transmission system is employed to increase the torque applied to the links and consequently to amplify the robot power. Most of controllers developed so far to control robot manipulators were based on the assumption of rigid joints; that is the transmission was assumed to be completely stiff, and it was also assumed that there was no difference between the angular positions of the driving actuator and that of the driven link.[1–6] However, it was experimentally shown that the assumption of rigid joints generally limits a robot's ability to perform high-speed high-precision manipulations,[7–12] and flexibility of the joints may produce lightly damped oscillatory motions. Especially, the effect of joint flexibility becomes more significant in robot manipulators driven by harmonic drives. While harmonic drives have zero backlash, high torque transmissibility and compact size,[13,14] there is high torsional elasticity in harmonic drives which limit their capability.[15] Therefore, a more accurate control strategy in which the joint flexibility is taken into account is essential, especially in applications such as robots used in the manufacture of precision components like circuit boards. However, because of the existence of inherent non-linearities in the dynamic equations of flexible manipulators, developing an accurate model is difficult.

In addition to joint flexibility, another important factor which affects the performance of robot manipulators is joint friction. It has been proven that joint friction can lead to tracking errors and undesired stick–slip motion, and affects both the dynamic and static behaviours of a robot manipulator at the start, during and at the end of the motion.[16–22] Despite this, joint friction is usually neglected in modelling and control strategies developed for flexible-joint manipulators, and most of the models developed for flexible-joint manipulators ignore joint friction. For instance in refs. [23] and [24] a control strategy is designed based on singular perturbation theory for tip trajectory tracking of flexible-joint manipulators. However, in these works the joint friction was not considered in the dynamics of the manipulator.

In this paper a novel control strategy is introduced for the tip trajectory tracking of a flexible-joint manipulator which includes two main parts:

1. Friction-compensating torque which is designed so as to compensate for the friction effect
2. Composite controller which is designed to compensate for the flexibility effect in the joints

To compensate for the friction effect in the joints, a new friction compensation strategy is introduced in this paper. The key advantage of this strategy is that the friction-compensating torque can be identified easily in two steps. In most friction models developed to predict the joint friction, an experimental identification procedure is necessary to determine the friction model parameters. This identification procedure involves a large number of experiments which need to be carried out at different velocities and require considerable amount of time. In the proposed model, the parameters of the compensation strategy are identified in only two steps, and hence, the proposed model is more cost-effective in terms of the experimental time required to identify the parameters of the controller.

* Corresponding author. E-mail: reza.fotouhi@usask.ca

https://doi.org/10.1017/S0263574709990373 Published online by Cambridge University Press

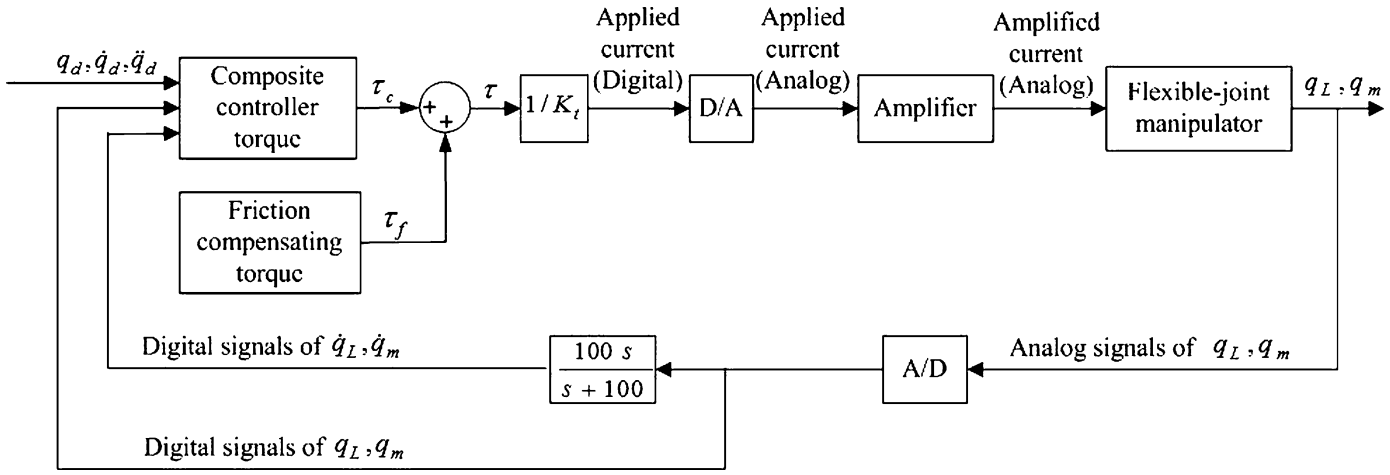



Fig. 1. Control strategy designed for tip trajectory of flexible-joint manipulator.

To compensate for the flexibility in the joints, a composite controller is designed based on the singular perturbation theory along with the integral manifold concept. In singular perturbation models developed for flexible-joint manipulators, e.g. in refs. [9] and [24], the inertias of the rotors are ignored; however, ignoring any parameters in the dynamics of a system leads to inaccuracy in the performance of the controller, since controllers whose design is based on the singular perturbation theory are model based. This error specifically becomes more important when high precision in control is expected. In this paper, a more accurate dynamic model, which takes into account the inertias of rotors including gear reduction, is presented. While considering the effect of rotors' inertias leads to a more detailed and more complex dynamic model, it improves the precision of the controller in trajectory tracking.

Finally, the developed control strategy is experimentally verified by the experimental set-up of a single rigid-link flexible-joint (SRLFJ) manipulator in the Robotics Laboratory at the University of Saskatchewan. Also, in order to assess the effectiveness of the model based on the work-energy principle, experiments were performed and compared using two friction-compensating strategies: a new method established based on the work-energy principle[25] and the LuGre method.[18]

## 2. Methodology

Figure 1 shows the schematic of the control strategy that was used in the control of flexible-joint manipulators. The desired trajectory $q_d$ and its derivatives $\dot{q}_d$ and $\ddot{q}_d$ were the inputs to the digital controller, and the rotation and velocity of the motor and link were used as feedback to the controller. The applied current was fed into the digital controller and the output digital signal to a digital to analogue (D/A) card. The analogue current signal was then amplified and applied to the plant which was a flexible-joint manipulator. The positions of the motor and link, $q_L$ and $q_m$[1], were measured using the encoders implemented in the experimental set-up, and the values of the velocity were then obtained by taking the derivative of the position signals using a filter. The applied torque $\tau = \tau_f + \tau_c$ had two parts: the friction-compensating torque $\tau_f$ and the composite torque $\tau_c$. The procedures of designing these torques are described in following sections. To calculate the current required by the motor, the resultant torque $\tau$ was multiplied by the inverse of the torque constant of the motor, $K_t$, and the current was then fed into a D/A card. The value of the motor torque constant for the experimental set-up was $K_t = 8.92\,\text{Nm/A}$.[2]

## 3. Friction Compensation in Harmonic Drives

In this section two different friction models are developed for the experimental set-up of SRLFJ manipulator. In the first model, joint friction $\tau_f$ is approximated as a function of velocity based on the LuGre model, $\tau_f^{\text{LG}}$.[18] For this purpose, the joint friction values are obtained at different velocities, and the joint friction torque is then estimated as a function of velocity by the curve-fitting method. In the second model, the friction-compensating torque is designed based on the work-energy principle as a feed-forward linear compensating torque, $\tau_f^{\text{WE}}$.

### 3.1. LuGre model

A typical friction model which describes different aspects of friction torque is the LuGre model. In this model, on the microscopic scale, surfaces sliding on each other are modelled as two rigid bodies that make contact through elastic bristles which model the random asperities[3] of the surfaces (see Fig. 2). The bristles start to deflect when one surface (upper surface) starts to move, and the force is then applied tangentially to the bristles of the lower surface. If the deflection is sufficiently large, the surfaces will slide on each

[1] The angle $q_m$ measures the rotor angle after gear reduction; however, for the purpose of abbreviation, it is referred to as the motor angle in this paper.

[2] It is noteworthy that DC permanent magnet motors usually have a linear relationship with motor torque.

[3] Regardless of how smooth a surface is, it has many random micro-scale irregularities which are called asperities.

https://doi.org/10.1017/S0263574709990373 Published online by Cambridge University Press

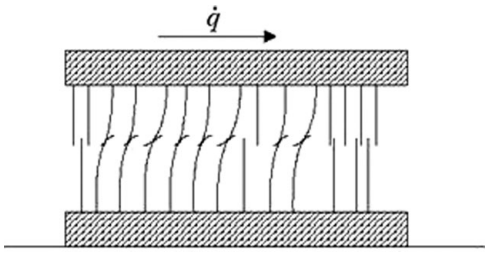



Fig. 2. Two surfaces are sliding on each other; the asperities are modelled as bristles attached to the surfaces.

other. The proposed model has the mathematical form[18]

$$\frac{\mathrm{d}y}{\mathrm{d}t} = \dot{q}_m - \sigma_0 \frac{|\dot{q}_m|}{g(\dot{q}_m)} y, \tag{1}$$

$$\tau_f^{\mathrm{LG}} = \sigma_0 y + \sigma_1 \frac{\mathrm{d}y}{\mathrm{d}t} + c_m \dot{q}_m, \tag{2}$$

where $y$ is the average deflection of the bristles and $\dot{q}_m$ is the relative velocity between surfaces; $\sigma_0$, $\sigma_1$ and $c_m$ are the stiffness of the bristles, damping of the bristles and viscous damping coefficient, respectively. Function $g(\dot{q}_m)$ represents the Stribeck effect which characterizes the transition between the static friction (stiction) and viscous friction, and $\tau_f^{\mathrm{LG}}$ is the friction torque modelled based on the LuGre method. Equations (1) and (2) are non-linear equations describing the friction behaviour based on the deflection of bristles. Since the average deflection of the bristles cannot be measured directly, finding the exact solution to predict the friction behaviour is not possible. However, Eqs. (1) and (2) can be simplified for the steady-state condition (sliding regime) in which the deformation rate of bristles is zero ($\mathrm{d}y/\mathrm{d}t = 0$).

Thus, from Eq. (1),

$$\sigma_0 y_{ss} = g(\dot{q}_m)\frac{\dot{q}_m}{|\dot{q}_m|} = \mathrm{sgn}(\dot{q}_m) g(\dot{q}_m), \tag{3}$$

where $y_{ss}$ is the steady-state value of the bristles deformation and the sign function is defined as

$$\mathrm{sgn}(\dot{q}_m) = \begin{cases} 1 & \dot{q}_m > 0, \\ -1 & \dot{q}_m < 0. \end{cases} \tag{4}$$

For steady-state condition, ($\mathrm{d}y/\mathrm{d}t = 0$), the friction torque is obtained by substituting Eq. (3) into Eq. (2):

$$\tau_f^{\mathrm{LG}} = \mathrm{sgn}(\dot{q}_m) g(\dot{q}_m) + c_m \dot{q}_m. \tag{5}$$

A typical proposed form for the function $g(\dot{q})$ is[18]

$$g(\dot{q}_m) = \tau_{fc}^{\mathrm{LG}} + \left(\tau_{fs}^{\mathrm{LG}} - \tau_{fc}^{\mathrm{LG}}\right) \mathrm{e}^{-(\dot{q}_m/v_s)^2}, \tag{6}$$

where $\tau_{fc}^{\mathrm{LG}}$ and $\tau_{fs}^{\mathrm{LG}}$ are the Coulomb friction and stiction torque respectively and $v_s$ is the Stribeck velocity. Replacing Eq. (6) in Eq. (5) leads to

$$\tau_f^{\mathrm{LG}}(\dot{q}_m, \psi) = \left[\tau_{fc}^{\mathrm{LG}} + \left(\tau_{fs}^{\mathrm{LG}} - \tau_{fc}^{\mathrm{LG}}\right) e^{-(\dot{q}_m/v_s)^2}\right] \times \mathrm{sgn}(\dot{q}_m) + c_m \dot{q}_m, \tag{7}$$

where $\psi$ is a vector which includes four constant parameters of the LuGre friction model; that is $\psi = [\tau_{fs}^{\mathrm{LG}} \tau_{fc}^{\mathrm{LG}} v_s c_m]$. The first and second terms of the friction torque in the above equation describe the Coulomb friction and Stribeck effect respectively, and the last term accounts for the viscous damping. To characterize friction torque as a function of velocity in Eq. (7), four unknown parameters, $\psi = [\tau_{fs}^{\mathrm{LG}}\ \tau_{fc}^{\mathrm{LG}}\ v_s\ c_m]$, must be identified. A schematic of the experimental procedure which was used to identify friction model parameters is shown in Fig. 3. The motor position was controlled by a proportional–integral–derivative (PID) controller to follow a triangular wave position reference. The dynamic equation of motor is expressed as

$$J\,\ddot{q}_m = \tau - \tau_f, \tag{8}$$

where $J$, $\tau$, $\tau_f$ and $\ddot{q}_m$ are the mass moment of inertia of the motor, applied torque, joint friction and acceleration of the motor respectively. If the motor follows the reference trajectory, which is a triangular trajectory with constant velocity, the motor acceleration $\ddot{q}_m$ will become zero, and as a result the applied torque will be equal to the actual friction torque in the above equation, i.e. $\tau = \tau_f$. Therefore, the friction torque can be determined by measuring the applied torque.

In total, 22 experiments were carried out in different steady-state velocities to estimate the friction torque. The experimental data were then interpolated (curve-fitted) with

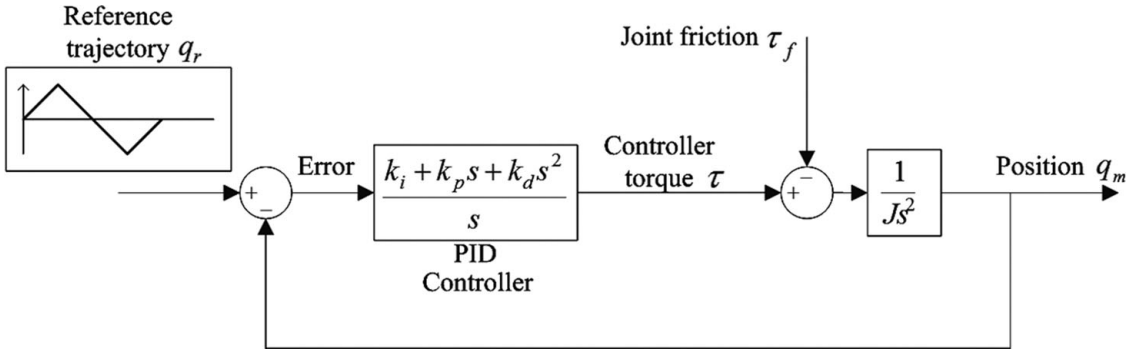



Fig. 3. Schematic of the control procedure used to identify the LuGre model parameters.

https://doi.org/10.1017/S0263574709990373 Published online by Cambridge University Press

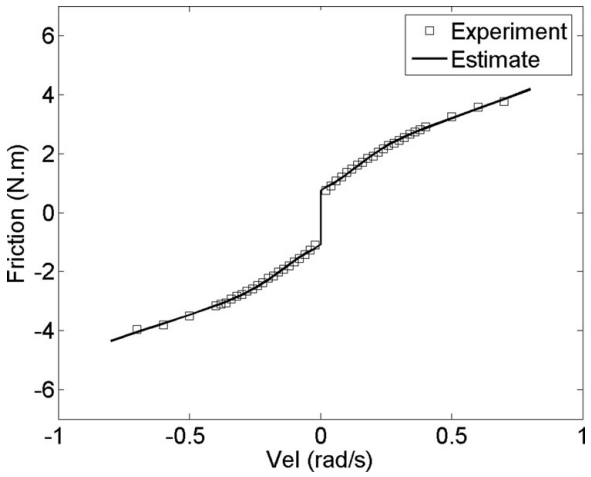



Fig. 4. Comparison of experimental results with friction torque obtained in Eq. (10) based on the LuGre model.

the LuGre friction torque $\tau_f^{\mathrm{LG}}$ given in Eq. (7). For this purpose, the non-linear optimization technique (MATLAB function *lsqcurvefit.m*) was used to minimize the quadratic cost function $I$ which was defined as

$$I = \sum_{i=1}^{N} \left[\tau_f\left(\dot{q}_m^{(i)}\right) - \tau_f^{\mathrm{LG}}\left(\dot{q}_m^{(i)}, \psi\right)\right]^2, \tag{9}$$

where $\tau_f(\dot{q}_m^{(i)})$ represents the actual joint friction torque which is measured experimentally during constant motor velocity $\dot{q}_m^{(i)}$. The torque $\tau_f^{\mathrm{LG}}(\dot{q}_m^{(i)}, \psi)$ is the joint friction torque which is modelled based on the LuGre model and is given in Eq. (7), and $N$ is the number of the measured data points. The cost function $I$ represents the error between experimental data points, $\tau_f(\dot{q}_m^{(i)})$, and the estimation function of LuGre model, $\tau_f^{\mathrm{LG}}(\dot{q}_m^{(i)}, \psi)$. Therefore, by minimizing cost function, optimum values of $\psi = [\tau_{fs}^{\mathrm{LG}}\ \tau_{fc}^{\mathrm{LG}}\ v_s\ c_m]$ can be found. These values were obtained as $\psi = [1.57\ -0.792\ 0.1903.26]$ and $\psi = [-1.99\ 0.847\ 0.199\ 2.93]$ for positive and negative velocities, respectively. By replacing the optimum values of the parameters in the LuGre model in the sliding regime, the friction torques can be expressed as functions of velocity:

$$\left.\begin{aligned} \tau_f^{\mathrm{LG}} &= [1.57 - 0.792\mathrm{e}^{-(\dot{q}_m/0.190)^2}] \\ &\quad \times \mathrm{sgn}(\dot{q}_m) + 3.26\dot{q}_m(\mathrm{Nm}),\ \dot{q}_m > 0, \\ \tau_f^{\mathrm{LG}} &= [-1.99 + 0.847e^{-(\dot{q}_m/0.199)^2}] \\ &\quad \times \mathrm{sgn}(\dot{q}_m) + 2.93\dot{q}_m(\mathrm{Nm}),\ \dot{q}_m < 0. \end{aligned}\right\} \tag{10}$$

Figure 4 shows the experimental, $\tau_f$, and estimated results of joint friction, $\tau_f^{\mathrm{LG}}$.

### 3.2. Friction model based on work-energy principle

In this section, a friction compensation strategy based on the work-energy principle is proposed. As shown in the previous section, the LuGre method, which is an approximate method for modelling the friction, requires a time-consuming identification procedure including a large number of experiments. Also, the friction torque defined in (10) is obtained based on the assumption of steady-state conditions. Therefore, it cannot model the pre-sliding regime in which the stick–slip motion occurs at very low velocities. Furthermore, the friction can change with oil temperature, load, humidity and actuator wear.[21] However, these effects are not taken into account in the friction model presented for the shoulder joint using the LuGre method. Another disadvantage of the LuGre torque given in Eq. (7) is that it assumes that the stiction at the beginning and end of the motion of the manipulator is the same, while in practice the stiction at the beginning of the manoeuvre is usually greater than that at the end. Here, a new approach is introduced for friction compensation which is identified in only two steps.

According to the work-energy principle, the work done during the motion of the flexible-joint robot manipulator includes the work done by the motor torque, $W_I$, the energies dissipated by viscous damping, $W_d$, and the Coulomb friction torque, $W_{df}$. The total work done by the output controller is composed of two parts, the work of the composite controller torque $\tau_c$, which is $W_{I_c}$, and the work of the compensating torque of dry friction $\tau_{fd}^{\mathrm{WE}}$, which is $W_{I_f}$. These works can be written as

$$\begin{aligned} W_I &= \int_0^{\theta_f} \tau\, \mathrm{d}q_m = \int_0^{t_f} \tau \dot{q}_m\, \mathrm{d}t = \int_0^{t_f} \left(\tau_c + \tau_{fd}^{\mathrm{WE}}\right)\dot{q}_m \mathrm{d}t \\ &= \int_0^{t_f} \tau_c \dot{q}_m\, \mathrm{d}t + \int_0^{t_f} \tau_{fd}^{\mathrm{WE}} \dot{q}_m\, \mathrm{d}t = W_{I_c} + W_{I_f}, \end{aligned} \tag{11}$$

where $\theta_f$ and $t_f$ are the final rotation of the joint and the time at which link reaches its final position, respectively, and $W_{I_c} = \int_0^{t_f} \tau_c \dot{q}_m\, \mathrm{d}t$ and $W_{I_f} = \int_0^{t_f} \tau_{fd}^{\mathrm{WE}} \dot{q}_m\, \mathrm{d}t$. The energy dissipated by the viscous damping is

$$W_d = \int_0^{\theta_f} c_m \dot{q}_m\, \mathrm{d}q_m = \int_0^{t_f} c_m \dot{q}_m^2\, \mathrm{d}t. \tag{12}$$

The energy dissipated by the dry Coulomb friction, $\tau_{fc}$, can be written as

$$W_{df} = \int_0^{\theta_f} \tau_{fc}\, \mathrm{d}q_m = \int_0^{t_f} \tau_{fc} \dot{q}_m\, \mathrm{d}t. \tag{13}$$

The principle of work and energy for a general system is

$$K_2 = \sum W_{1\to 2} + K_1, \tag{14}$$

where $\sum W_{1\to 2}$ expresses the total work done by the forces (conservative and non-conservative) on the system from the initial position 1 to the final position 2 and $K_1$ and $K_2$ are total kinetic energy of the system at the initial and final positions, respectively. Since the velocity is zero at the initial and final positions, $K_1$ and $K_2$ are zero and Eq. (14) reduces to

$$\sum W_{1\to 2} = 0. \tag{15}$$

Thus

$$\sum W_{1\to 2} = W_{I_c} + W_{I_f} - W_d - W_{df} = 0 \tag{16}$$

https://doi.org/10.1017/S0263574709990373 Published online by Cambridge University Press

and the work done by $\tau_{fd}^{\mathrm{WE}}$ can be obtained as

$$W_{I_f} = -W_{I_c} + W_d + W_{df}. \tag{17}$$

Hence,

$$\int_0^{t_f} \tau_{fd}^{\mathrm{WE}} \dot{q}_m \, \mathrm{d}t = -W_{I_c} + W_d + W_{df}. \tag{18}$$

The friction-compensating torque, $\tau_{fd}^{\mathrm{WE}}$, can now be obtained from Eq. (18). There are many candidates for the friction-compensating torque function which satisfies Eq. (18). For convenience, the friction-compensating torque was assumed to be of linear form, that is

$$\tau_{fd}^{\mathrm{WE}} = \begin{cases} a + bt, & 0 < t < -(a/b), \\ 0, & t > -(a/b). \end{cases} \tag{19}$$

Thus, Eq. (18) becomes

$$\int_0^{t_f} (a + bt)\dot{q}_m \, \mathrm{d}t = -W_{I_c} + W_d + W_{df}. \tag{20}$$

Parameter $a$ is the torque required to overcome stiction and initiate motion of the manipulator from the rest position. The parameter $b$ can then be obtained using above equation. The friction torque obtained in Eq. (19) includes the dry friction effect. To obtain the total friction torque, the viscous friction effect $c_m\dot{q}_m$ must be added to the torque in Eq. (19), and hence

$$\tau_f^{\mathrm{WE}} = \begin{cases} a + bt + c_m\dot{q}_m, & 0 < t < -(a/b), \\ c_m\dot{q}_m, & t > -(a/b), \end{cases} \tag{21}$$

where $\tau_f^{\mathrm{WE}}$ is the joint friction torque which includes dry and viscous effects. While the friction torque obtained based on the work-energy principle in Eq. (21) has fewer parameters and a simpler form compared to the LuGre model in Eq. (10), it is more accurate in compensating for the friction. For instance the experimental results in Section 5.2 for an SRLFJ show that by using $\tau_f^{\mathrm{WE}}$ the trajectory tracking error is significantly reduced in contrast to the results obtained by using the LuGre method.

## 4. Composite Controller

In this section, a composite controller is designed for tip trajectory tracking of flexible-joint manipulators. In the composite controllers developed so far to control flexible-joint manipulators, the dynamic coupling between the actuators and the links is ignored (e.g. refs. [9] and [24]). This leads to the fact that the off-diagonal terms in the mass matrix in the dynamic model become zero, and the dynamic model of flexible-joint manipulator is simplified. However, ignoring the coupling between the actuators and the links leads to the error in the performance of the controller, since in singular perturbation theory the controller is model based and any error in the dynamic model causes the deficiency in the control performance. To remove this error, all coupling effects between the actuators and the links are considered in the dynamic model developed in this paper, and consequently it provides more accuracy in the control of flexible-joint manipulators.

### *4.1. Singularly perturbed systems*

The standard governing equations of a singularly perturbed system are[26,27]

$$\dot{X} = f(X, Z, \varepsilon, t), \quad X(t_0) = X^0, \quad X \in R^n, \tag{22}$$

$$\varepsilon \dot{Z} = g(X, Z, \varepsilon, t), \quad Z(t_0) = Z^0, \quad Z \in R^m, \tag{23}$$

where $\varepsilon$ represents a small parameter; $X$ and $Z$ are state vectors of dimensions $n$ and $m$, respectively; $f \in R^n$; $g \in R^m$; and $\dot{X}$, $\dot{Z}$ are the time derivatives and, $X^0$ and $Z^0$ are the initial conditions of states $X$ and $Z$, respectively. State $Z$is called the *fast state* of the system because $\varepsilon$ is a small parameter and the time variation of $Z$ is very large (Eq. (23)). In contrast, state $X$ is called the *slow state* of the system because it has a slower time variation compared with state $Z$.

For Eqs. (22) and (23), which represent the $(n+m)$-dimensional state-space equations of $X$ and $Z$, depending on the parameter $\varepsilon$, there is an integral manifold $M_\varepsilon$ which represents the $m$-dimensional set of equations and is defined as

$$M_\varepsilon : Z = \varphi(X, \varepsilon), \quad X \in R^n, Z \in R^m, \tag{24}$$

where $\varphi$ is a function of state $X$ and time. Since $Z$ in Eq. (24) is the solution of Eq. (23), it has to satisfy the following integral manifold condition:

$$\varepsilon \dot{Z} = \varepsilon \frac{\partial \varphi}{\partial X} f(X, \varphi(X, \varepsilon)) = g(X, \varphi(X, \varepsilon)). \tag{25}$$

If Eq. (25) is satisfied, fast states $Z$ can be replaced by the integral manifold $\varphi(X, \varepsilon)$ in Eq. (22). This leads to

$$\dot{X} = f(X, \varphi(X, \varepsilon), \varepsilon, t), \quad X(t_0) = X^0, \quad X \in R^n. \tag{26}$$

The resultant model in Eq. (26) is called the reduced-order model, since it includes only the slow states $X$ and has an order of $n$ compared to the original system, Eqs. (22) and (23), which has an order of $(n + m)$. Thus, as long as the fast state $Z$ moves on the integral manifold, that is $Z = \varphi(X, \varepsilon)$, instead of the original system, Eqs. (22) and (23), the reduced-order model, Eq. (26), can be used to describe the dynamics of the slow states. On the other hand, if Eq. (25) is not satisfied there will be the difference $\eta$ between $Z$ and $\varphi$, i.e. $\eta = Z - \varphi(X, \varepsilon)$. In the control approach based on the integral manifold, two controllers are designed. The first one, called the fast controller, is designed to remove the difference between the fast state and the integral manifold, and as a result $\eta \to 0$ and $Z = \varphi(X, \varepsilon)$. The second controller, the slow controller, is designed to control the slow states in the reduced-order model (Eq. (26)). Therefore, using the singular perturbation theory along with the integral manifold concept allows for decomposing the system into fast and slow subsystems, and controllers are then designed for each subsystem separately.

https://doi.org/10.1017/S0263574709990373 Published online by Cambridge University Press

Fast and slow subsystems can be obtained from the singularly perturbed equations of the system, Eqs. (22) and (23), in terms of $X$ and $\eta$:

$$\dot{X} = f(X, \varphi(X, \varepsilon) + \eta), X(t_0) = X^0, \tag{27}$$

$$\varepsilon\,\dot{\eta} = \varepsilon\,\dot{Z} - \varepsilon\,\dot{\varphi}(X, \varepsilon) = \varepsilon\dot{Z} - \varepsilon\frac{\partial\varphi(X, \varepsilon)}{\partial\,X}\dot{X}$$

$$= g(X, \varphi(X, \varepsilon) + \eta) - \varepsilon\frac{\partial\varphi(X, \varepsilon)}{\partial X} f(x, \varphi(X, \varepsilon) + \eta),$$

$$\eta(t_0) = \eta^0, \tag{28}$$

where $\eta^0$ is the vector of the initial condition of the fast states $\eta$. In fact, Eq. (27) describes the slow variations of the state $X$, and Eq. (28) represents the dynamic of the fast state $\eta$. It is clear that if $\eta = 0$, Eq. (28) will be the same as Eq. (25), which means that the manifold condition is satisfied and $Z$ moves on its manifold.

### *4.2. Singularly perturbed model of flexible-joint manipulators*

The dynamic equations of a serial manipulator consisting of $n$ rigid links connected by $(n - 1)$ elastic joints are described by the following set of differential equations:

$$D(q_L)\ddot{q}_L + C_l(q_L, \dot{q}_L)\dot{q}_L + K(q_L - q_m) = H(\tau - \tau_f), \tag{29}$$

$$J\,\ddot{q}_m - K(q_L - q_m) = \tau - \tau_f, \tag{30}$$

where $D(q_L) \in R^{n\times n}$ is the inertia matrix of the links; $C_l(q_L, \dot{q}_L)\dot{q}_L$ represents the Coriolis and centrifugal effects; $K \in R^{n\times n}$, defined as $K = \text{diag}(k_1, \ldots, k_n)$, represents the stiffness of the joints; $J \in R^{n\times n}$ is the inertia matrix of the motors; and $\tau$ is the vector of applied torques through the motors, respectively. Also, $q_L \in R^n$ and $q_m \in R^n$ represent, respectively, the rotations of the links and the motors. The components of matrix $H$ are defined as $H_{ij} = -1$ when $i = j - 1$ and $H_{ij} = 0$ when $i \neq j - 1$. The correctness of dynamic equations (29) and (30) has been verified using finite-element analysis (FEA) for the two-rigid-link flexible-joint manipulator ($n = 2$). The details are given in Appendix A.

As stated earlier, the applied torque $\tau$ includes two parts: composite torque $\tau_c$ and friction-compensating torque $\tau_f$. That is

$$\tau = \tau_c + \tau_f. \tag{31}$$

As a result, the joint friction can be eliminated from the dynamic equations of the manipulator, and hence,

$$D(q_L)\ddot{q}_L + C_l(q_L, \dot{q}_L)\dot{q}_L + K(q_L - q_m) = H\tau_c, \tag{32}$$

$$J\,\ddot{q}_m - K(q_L - q_m) = \tau_c. \tag{33}$$

In the following, the application of the singular perturbation theory and the integral manifold concept is applied to control flexible-joint manipulators. Based on the singular perturbation approach, the system is first decomposed into two subsystems, slow and fast, and controllers are then designed for each subsystem. The slow subsystem represents the low-frequency motion of the flexible manipulator in which the working frequency range depends on the flexibility of the joints. For instance if the joint flexibility goes to infinity, the slow subsystem reduces to a rigid manipulator in which the manipulator manoeuvre will be a rigid body motion (zero frequency). The fast subsystem deals with the motion of the manipulator at higher frequency vibration.

If all the spring constants $k_i$ are assumed to be of the same order of magnitude, they can be written as a multiple of a single large parameter $\bar{k}$,

$$k_i = \bar{k}\,\tilde{k}_i, i = 1, \ldots, n, \tag{34}$$

and the elastic joint torque is

$$\xi = \bar{k}\tilde{K}(q_L - q_m), \tag{35}$$

where

$$\tilde{K} = \text{diag}(\tilde{k}_1, \ldots, \tilde{k}_n).$$

Without loss of generality (by rescaling the $\xi$ variables if necessary), the matrix $\tilde{K}$ is chosen as $\tilde{K} = I$. The singular perturbation parameter can now be defined as $\mu = 1/\bar{k}$, and Eq. (35) becomes

$$\mu\xi = q_L - q_m. \tag{36}$$

Then by using Eq. (36), Eqs. (32) and (33) become

$$\ddot{q}_L = -D^{-1}(C_l\dot{q}_L + \xi - H\tau_c), \tag{37}$$

$$\ddot{q}_m = J^{-1}(\xi + \tau_c). \tag{38}$$

Setting $x = q_1$ and subtracting Eq. (38) from (37), one obtains

$$\ddot{x} = -D^{-1}(C_l\dot{x} + \xi - H\tau_c), \tag{39}$$

$$\mu\ddot{\xi} = J^{-1}[-\xi + (JD^{-1}H - I)\tau_c] - D^{-1}(C_l\dot{x} + \xi). \tag{40}$$

Equations (39) and (40) represent the singularly perturbed model of the flexible-joint manipulators. These equations can be written as

$$\ddot{x} = a_1(x, \dot{x}) + a_2(x)\xi + a_3(x)\tau_c, \tag{41}$$

$$\mu\ddot{\xi} = b_1(x, \dot{x})\dot{x} + b_2(x)\xi + b_3(x)\tau_c, \tag{42}$$

where

$$a_1(x, \dot{x}) = -D^{-1}C_l\dot{x},\ a_2(x) = -D^{-1},$$

$$a_3(x) = D^{-1}H, b_1(x, \dot{x}) = -D^{-1}C_l,$$

$$b_2(x) = -(J^{-1} + D^{-1}), b_3(x) = D^{-1}H - J^{-1}.$$

Moreover, the state-space representation of the singularly perturbed system, Eqs. (41) and (42), can be obtained by choosing $x_1 = x$, $x_2 = \dot{x}$, $z_1 = \xi$ and $z_2 = \varepsilon\dot{\xi}$, where $\varepsilon = \sqrt{\mu}$. Thus

https://doi.org/10.1017/S0263574709990373 Published online by Cambridge University Press

$$\dot{X} = A_1(X) + A_2(X)Z + A_3(X)\tau_c, \tag{43}$$

$$\varepsilon \dot{Z} = B_1(X)X + B_2(X)Z + B_3(X)\tau_c, \tag{44}$$

where

$$X = [x_1\ x_2]^T_{1\times 2n},\ Z = [z_1 \quad z_2]^T_{1\times 2n},$$

$$A_1 = \begin{bmatrix} x_2 \\ a_1(x_1, x_2) \end{bmatrix}_{2n\times 1},\ A_2 = \begin{bmatrix} O_{n\times n} & O_{n\times n} \\ a_2(x_1) & O_{n\times n} \end{bmatrix}_{2n\times 2n},$$

$$A_3 = \begin{bmatrix} O_{n\times n} \\ a_3(x) \end{bmatrix}_{2n\times n},$$

$$B_1 = \begin{bmatrix} O_{n\times n} & O_{n\times n} \\ O_{n\times n} & b_1(x_1, x_2) \end{bmatrix}_{2n\times 2n},$$

$$B_2 = \begin{bmatrix} O_{n\times n} & I_{n\times n} \\ b_2(x_1, x_2) & O_{n\times n} \end{bmatrix}_{2n\times 2n},$$

$$B_3 = \begin{bmatrix} O_{n\times n} \\ b_3(x_1, x_2) \end{bmatrix}_{2n\times n}.$$

*4.2.1. Recovery of the rigid robot manipulator.* In the following it will be shown that by setting $\mu = 0$ the equation of motion of the rigid manipulator will be recovered. In an ideal rigid manipulator, joints stiffness must tend to infinity, i.e. $K \to \infty$, and as a result $\mu \to 0$. Therefore, the flexible-joint manipulator in Eqs. (41) and (42) must behave as a rigid manipulator when $\mu = 0$. Setting $\mu = 0$ in Eqs. (41) and (42) leads to

$$\ddot{x} = a_1(x, \dot{x}) + a_2(x)\xi + a_3(x)\tau_c, \tag{45}$$

$$0 = b_1(x, \dot{x})\dot{x} + b_2(x)\xi + b_3(x)\tau_c. \tag{46}$$

Solving (46) for $\xi$ and substituting the result in (45) leads to

$$\ddot{x} = a_1(x, \dot{x}) - a_2(x)b_2^{-1}(x)[b_1(x, \dot{x})\dot{x} + b_3(x)\tau_c] + a_3(x)\tau_c \tag{47}$$

Employing the definitions of $a_1$, $a_2$, $b_1$, $b_2$ and $b_3$, Eq. (47) becomes

$$\ddot{x} = -D^{-1}C_l\dot{x} + D^{-1}(J^{-1} + D^{-1})^{-1} \times [D^{-1}C_l\dot{x} + (J^{-1} - D^{-1}H)\tau_c] + D^{-1}H\tau_c, \tag{48}$$

and after some algebraic manipulations, Eq. (48) yields (see Appendix B for details)

$$\ddot{x} = (J + D)^{-1}[-C_l\dot{x} + (H + I)\tau_c] \tag{49}$$

which are the dynamic equations of the counterpart of the flexible-joint manipulator when the joints are rigid.[28]

*4.2.2. Integral manifold implementation.* According to the definition of the integral manifold in Eq. (24), an integral manifold for a flexible-joint manipulator in the space $R^{2n}$ is

$$M_\varepsilon : Z = \varphi(X, \tau_c, \varepsilon, t); X \in R^{2n}. \tag{50}$$

If $Z$ moves on the integral manifold, $Z$ can be substituted by the integral manifold $\varphi$ in Eq. (44), and therefore

$$\varepsilon \dot{\varphi} = B_1(X)X + B_2(X)\varphi + B_3(X)\tau_c. \tag{51}$$

The reduced-order model of the system is then

$$\dot{X} = A_1(X) + A_2(X)\varphi + A_3(X)\tau_c. \tag{52}$$

As discussed in Section 2, as long as $Z$ is on the integral manifold $\varphi$, the original governing equations of the system, Eqs. (43) and (44), reduce to its reduced-order model, Eq. (52). Thus, provided that the fast state $Z$ is restricted to move on the integral manifold, the controller can be only designed to control the slow state $X$in Eq. (52). It is a very significant advantage of using the integral manifold concept because the controller will be designed for the reduced-order model of dimension $n$, while the original system has a dimension of $n + m$. The design procedure of the controller is discussed in the following section.

*4.2.3. Composite controller design procedure.* Here, a composite controller torque which consists of slow and fast controllers is proposed. The slow controller $\tau_{c,s}$ is designed to control the slow subsystem which presents the low-frequency motion of the manipulator. If the joint flexibility goes to infinity, the slow subsystem reduces to a rigid manipulator and the slow controller will be equal to the controller torque for the rigid manipulator, $\tau_{c,0}$, which can be obtained by using the inverse-dynamic approach.[29] The fast controller $\tau_{c,f}$ is selected to suppress the high-frequency vibration of the manipulator. Thus the composite controller $\tau_c$ can be written as the summation of slow and fast controller torques as

$$\tau_c = \tau_{c,s}(X, Z, \dot{X}, \dot{Z}) + \tau_{c,f}(X, Z, \dot{X}, \dot{Z}). \tag{53}$$

The difference between $Z$ and the integral manifold $\varphi$ is

$$\eta = Z - \varphi(X, \tau_{c,s}, \varepsilon, t), \tag{54}$$

and replacing Eqs. (44) and (51) in Eq. (54) results in

$$\begin{aligned} \varepsilon\dot{\eta} &= \varepsilon \dot{Z} - \varepsilon\dot{\varphi}(X, \tau_{c,s}, \varepsilon, t) \\ &= B_1(X)X + B_2(X)Z + B_3(X)\tau_c \\ &\quad - \{B_1(X)X + B_2(X)\varphi + B_3(X)\tau_{c,s}\} \\ &= B_2(X)\eta + B_3(X)\tau_{c,f} \end{aligned} \tag{55}$$

It is worth noting that once $Z$ is on the integral manifold, $\eta$ will be zero, and as a result $\tau_{c,f}$ will be zero and the control torque will have only the slow controller, i.e. $\tau_c = \tau_{c,s}(X, Z, \dot{X}, \dot{Z})$.

From Eqs. (43) and (55) the equations of the slow and fast subsystems in state space are

$$\dot{X} = A_1(X) + A_2(X)\varphi + A_2(X)\eta + A_3(X)\tau_c, \tag{56}$$

$$\varepsilon\dot{\eta} = B_2(X)\eta + B_3(X)\tau_{c,f}. \tag{57}$$

Equation (56) describes the low-frequency motion of the robot manipulator, and Eq. (57) represents the high-frequency motion of the robot manipulator.

https://doi.org/10.1017/S0263574709990373 Published online by Cambridge University Press

*Designing slow controller.* In this section, the slow controller $\tau_{c,s}$ is designed using perturbation method. For this purpose, the integral manifold $\varphi$ and the slow controller $\tau_{c,s}$ are expanded in terms of $\varepsilon$

$$\varphi_{c,s} = \varphi_0 + \varepsilon\varphi_1 + \varepsilon^2\varphi_2 + \ldots, \tag{58}$$

$$\tau_{c,s} = \tau_{c,0} + \varepsilon\tau_{c,1} + \varepsilon^2\tau_{c,2} + \ldots. \tag{59}$$

For a manipulator with rigid joints (i.e. $\varepsilon \to 0$), the slow controller reduces to $\tau_{c,0}$ which can be designed based on the conventional methods available for the rigid manipulators such as the inverse-dynamic approach.[29] In order to determine the other parts of the slow controller (i.e. $\tau_{c,1}, \tau_{c,2}, \ldots$), Eqs. (58) and (59) are substituted into integral manifold condition, Eq. (51). Therefore,

$$\begin{aligned}\varepsilon(\dot\varphi_0 + \varepsilon\dot\varphi_1 + \varepsilon^2\dot\varphi_2 + \ldots) &= B_1(X)X \\ &+ B_2(X)(\varphi_0 + \varepsilon\varphi_1 + \varepsilon^2\varphi_2 + \ldots) \\ &+ B_3(X)(\tau_{c,0} + \varepsilon\,\tau_{c,1} + \varepsilon^2\tau_{c,2} + \ldots).\end{aligned} \tag{60}$$

Equating the coefficients with the same power of $\varepsilon$ leads to

$$0 = B_1(X)X + B_2(X)\varphi_0 + B_3(X)\tau_{c,0}, \tag{61}$$

$$\dot\varphi_0 = B_2(X)\varphi_1 + B_3(X)\,\tau_{c,1}, \tag{62}$$

$$\dot\varphi_1 = B_2(X)\varphi_2 + B_3(X)\tau_{c,2}, \tag{63}$$

$$\dot\varphi_i = B_2(X)\varphi_{i+1} + B_3(X)\,\tau_{c,i+1}, \quad i = 2, 3, \ldots. \tag{64}$$

From Eq. (61) to Eq. (64), $\varphi_0$, $\varphi_1$ and $\varphi_i$ , $i = 2, 3, \ldots$, will be found in terms of $\tau_{c,i}$, iteratively. From Eq. (61)

$$\varphi_0 = -B_2^{-1}(X)[B_1(X)X + B_3(X)\tau_{c,0}]. \tag{65}$$

According to the definition of matrices $B_1$, $B_3$ and $B_4$, the last $n$ components of vector $\varphi_0 \in R^{2n}$ are zero; that is $\varphi_0$ can be written as

$$\varphi_0 = [(\varphi_{01})_{n\times 1} \quad O_{n\times 1}]_{2n\times 1}, \tag{66}$$

where $\varphi_{01}$ represents first $n$ components of vector $\varphi_0 \in R^{2n}$. If the second part of integral manifold, $\varphi_1$, is written as

$$\varphi_1 = [(\varphi_{11})_{n\times 1} \quad (\varphi_{12})_{n\times 1}]_{2n\times 1} \tag{67}$$

using the definition of the matrices $B_1$, $B_2$ and $B_3$, Eq. (65) leads to

$$\left.\begin{aligned}\dot\varphi_{01} &= \varphi_{12}, \\ 0 &= b_2(X)\varphi_{11} + b_3(X)\,\tau_{c,1}.\end{aligned}\right\} \tag{68}$$

By setting $\tau_{c,1} = 0$, $\varphi_{11}$ becomes zero in Eq. (68). Also, substituting $\varphi_1$ in Eq. (63) results in

$$\left.\begin{aligned}0 &= \varphi_{22}, \\ \dot\varphi_{12} &= b_2(X)\,\varphi_{21} + b_3(X)\tau_{c,2},\end{aligned}\right\} \tag{69}$$

where $\varphi_{21}$ and $\varphi_{22}$ represent, respectively, the first and second $n$ components of vector $\varphi_2 \in R^{2n}$. If $\tau_{c,2}$ is now chosen as

$$\tau_{c,2} = b_3^{-1}\dot\varphi_{12}, \tag{70}$$

then from Eq. (69) $\varphi_{21} = 0$ and consequently $\varphi_2 = 0$. Also, the terms containing $\varphi_i$, $i = 3, 4, \ldots$, will become zero by setting $\tau_{c,i} = 0$, $i = 3, 4, \ldots$, in Eq. (64). Therefore

$$\varphi_i = 0, \quad i = 3, 4, \ldots. \tag{71}$$

Consequently, from Eqs. (58) and (59), the terms of $\varphi$ and $\tau_{c,s}$ are expressed in the following form:

$$\varphi = \varphi_0 + \varepsilon\varphi_1, \tag{72}$$

$$\tau_{c,s} = \tau_{c,0} + \varepsilon^2 b_3^{-1}\dot\varphi_{12}. \tag{73}$$

*Designing fast controller.* As discussed in Section 4.1, the fast controller must be selected so that the difference between the integral manifold and parameter $Z$ asymptotically goes to zero; that is $\eta \to 0$. If the fast controller $\tau_{c,f}$ is chosen to have the state-feedback format

$$\tau_{c,f} = B_4\eta, \tag{74}$$

where $B_4$ is a constant matrix, then Eq. (57) becomes

$$\varepsilon\dot\eta = [B_2(X) + B_3(X)]B_4\eta. \tag{75}$$

If the elements of matrix $B_4$ are chosen so that the eigenvalues of the square matrix $[B_2(X) + B_3(X)B_4]$ always have negative real parts, the deviation of $Z$ from its manifold will asymptotically go to zero and, finally, $Z$ will be on its invariant manifold.

## 5. Experimental Verification

In order to verify the design of the controller described in the previous section, the experimental SRLFJ manipulator available at the Robotics Laboratory of the University of Saskatchewan was used. Figure 5 shows the experimental module of the SRLFJ that was used.

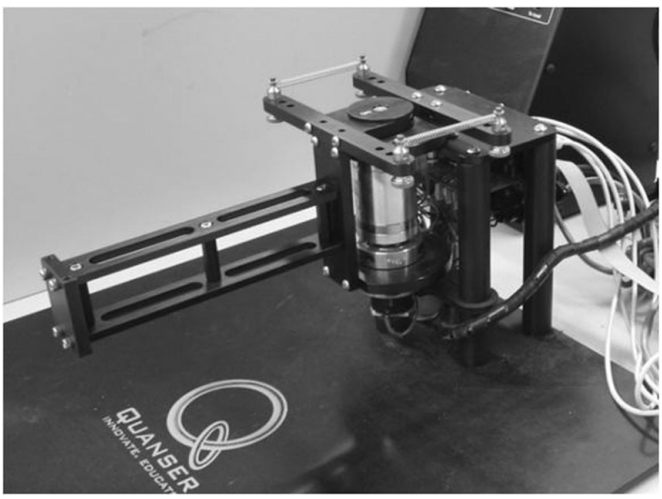



Fig. 5. Experimental module SRLFJ manipulator used.

https://doi.org/10.1017/S0263574709990373 Published online by Cambridge University Press

### *5.1. Experimental set-up*

The experimental module of the SRLFJ included a servo harmonic drive and a rigid link, as well as two parallel linear springs to represent the joint stiffness. Since the parallel springs applied a torque proportional to $(q_L - q_m)$, they were modelled as a torsional spring. The numerical values of the experimental set-up parameters were

$$j_L = 0.209 \text{ kg m}^2,\ j_m = 0.0110 \text{ kg m}^2,$$

$$c_m = 3.26 \text{ N m s/rad}, \text{k} = 10.3 \text{ N m/rad},\ l = 0.223 \text{ m},$$

where $j_L$, $j_m$ and $l$ are, respectively, the mass moment of inertias of the link and motor and the length of the link. The moments of inertias of the link and motor were calculated using the computer-aided design model and the information provided by the manufacturer of the motor, respectively. The viscous damping of the motor was determined from the torque impulse test.

Four different trajectories were chosen to verify the performance of the controller at different velocities and accelerations. These trajectories were

$$q_d^{(1)} = [70(t/t_f)^9 - 315(t/t_f)^8 + 540(t/t_f)^7 - 420(t/t_f)^6 + 126(t/t_f)^5]\theta_f, \quad (76)$$

$$q_d^{(2)} = [-20(t/t_f)^7 + 70(t/t_f)^6 - 84(t/t_f)^5 + 35(t/t_f)^4]\theta_f, \quad (77)$$

$$q_d^{(3)} = [6(t/t_f)^5 - 15(t/t_f)^4 + 10(t/t_f)^3]\theta_f, \quad (78)$$

$$q_d^{(4)} = [-2(t/t_f)^3 + 3(t/t_f)^2]\theta_f, \quad (79)$$

where the final position was $\theta_f = 0.5$ rad and the time required to reach the final position was $t_f = 2$ s. In all of these trajectories the motion of the manipulator started from $q_d^{(i)}(0) = \dot{q}_d^{(i)}(0) = 0, i = 1, 2, 3, 4$, and reached the final position at which $q_d^{(i)}(t_f) = \theta_f$, $\dot{q}_d^{(i)}(t_f) = 0, i = 1, 2, 3, 4$. Furthermore, the first and second proposed trajectories were designed such that $d^i q_d^{(1)}/dt^i = 0, i = 2, 3, 4$, and $d^i q_d^{(1)}/dt^i = 0, i = 2, 3$, at $t = 0$ and at $t = t_f$, respectively. Also, for the third trajectory the acceleration of the manipulator was set to zero at $t = 0$ and $t = t_f$. The experimental results for each of these desired trajectories are shown in Section 5.2.

### *5.2. Friction-compensating torque*

Based on the approach discussed in Section 3, two compensating friction torques were designed based on the work-energy principle and the LuGre method. To design a friction-compensating torque based on the work-energy principle, as discussed in Section 3.2, two parameters, $a$ and $b$, must be identified to determine the friction-compensating torque $\tau_{fd}^{\text{WE}} = a + bt$ in Eq. (19). Parameter $a$, the breakaway force, was obtained experimentally by increasing the torque gradually, until the manipulator started to move, as shown in Fig. 6. This torque was about 1.2 N m. To obtain the parameter $b$ from Eq. (20), the work of the composite controller torque and the dissipated energies by coulomb dry friction and viscous damping during motion of the manipulator were calculated using Eqs. (11)–(13) respectively. The values of work $W_{I_c}$, $W_d$ and $W_{df}$ were obtained experimentally by calculating the areas under the curves in Figs. 7–9 as

$$W_{I_c} = 1.0377 \text{ J}, \quad W_d = 0.6995 \text{ J}, \quad W_{df} = 0.4975 \text{ J}. \quad (80)$$

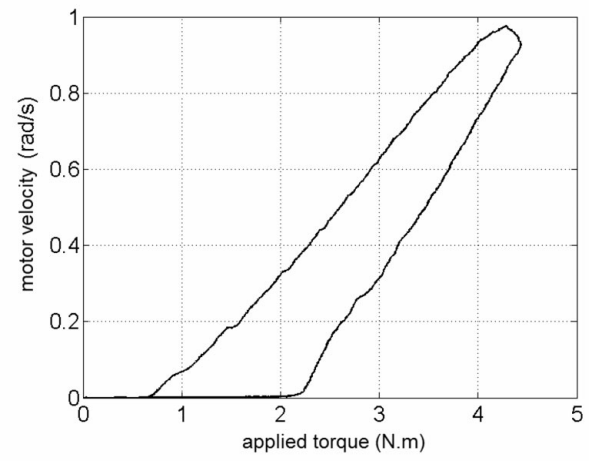



Fig. 6. The motor velocity response corresponding to the applied triangle torque to obtain experimentally $a$ in Eq. (19).

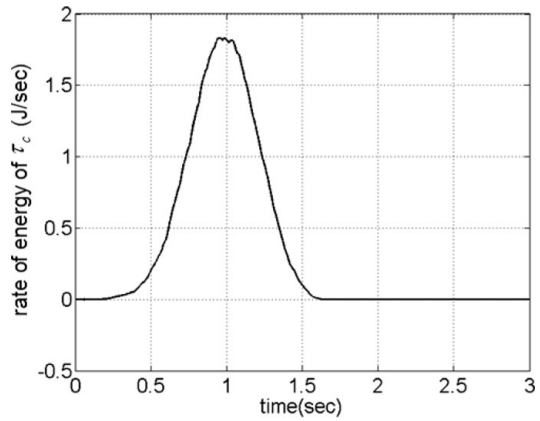



Fig. 7. The rate of the energy of the controller torque $\tau_c$ applied to the flexible-joint manipulator to obtain $W_{I_m}$ from Eq. (11) for manoeuvre $\theta_f = 0.5$ rad during 2 s.

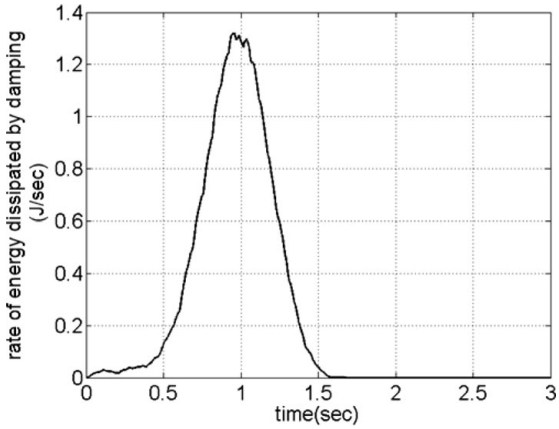



Fig. 8. The rate of the dissipated energy by viscous damping to obtain $W_d$ from Eq. (12) for manoeuvre $\theta_f = 0.5$ rad during 2 s.

https://doi.org/10.1017/S0263574709990373 Published online by Cambridge University Press

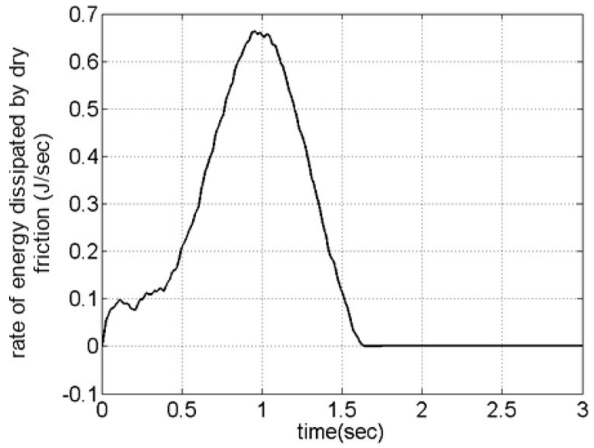



Fig. 9. The rate of the dissipated energy by dry friction to obtain $W_{df}$ from Eq. (13) for manoeuvre $\theta_f = 0.5$ rad during 2 s.

From Eq. (17), the work of the compensating friction torque must be

$$W_{I_f} = 0.1574 \text{ J}. \tag{81}$$

Finally by solving numerically Eq. (20), coefficient $b$ can be obtained as

$$b = -0.9941 \text{ N m/s}. \tag{82}$$

Therefore, based on the work-energy principle explained in Section 3.2 and according to Eq. (21) the friction-compensating torque including the viscous friction became

$$\tau_f^{\mathrm{WE}(1)} = -t + 1.2 + 3.26\dot{q}_m \text{ N m}. \tag{83}$$

Also, two other friction-compensating torques were selected as

$$\tau_f^{\mathrm{WE}(2)} = -1.2t + 1.2 + 3.26\dot{q}_m \text{ N m}, \tag{84}$$

$$\tau_f^{\mathrm{WE}(3)} = -0.8t + 1.2 + 3.26\dot{q}_m \text{ N m} \tag{85}$$

to ensure that the parameter $b$ was selected properly in Eq. (82). Another compensating torque was

$$\tau_f^{\mathrm{LG}} = 1.57 - 0.792\mathrm{e}^{-(\dot{q}_m/0.190)^2} + 3.26\,\dot{q}_m \text{ N m} \tag{86}$$

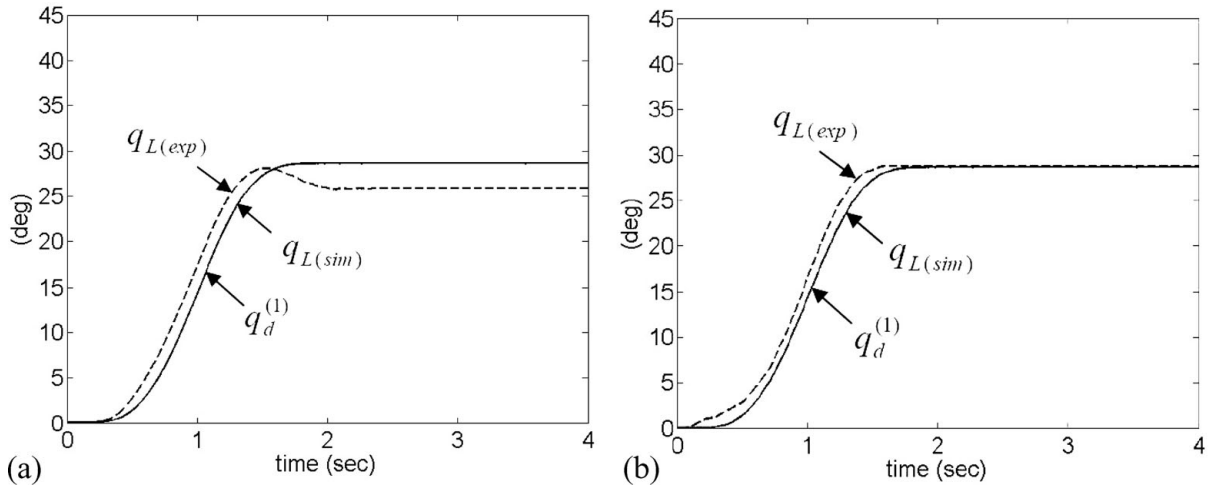



Fig. 10. Comparing simulation and experimental results of manipulator manoeuvre using composite controller and different friction compensation torques, (a) $\tau_f^{\mathrm{LG}}$ in Eq. (86), (b) $\tau_f^{\mathrm{WE}(1)}$ in Eq. (83) (link angle $q_L$ and the first desired trajectory $q_d^{(1)}$).

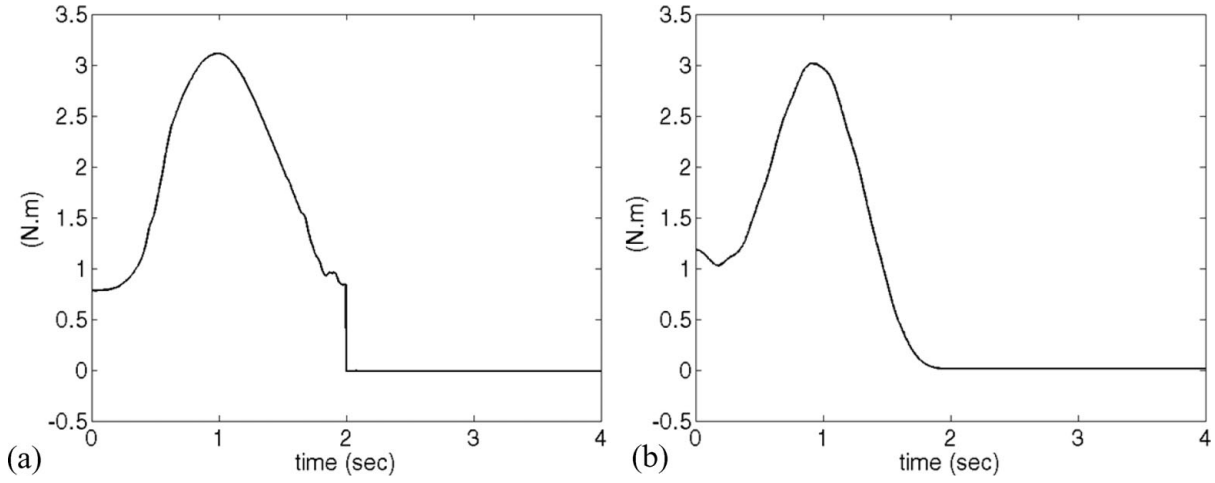



Fig. 11. Applied torque to the flexible-joint manipulator of motions in Fig. 10: (a)$\tau_{c,s} + \tau_f^{\mathrm{LG}}$, (b) $\tau_{c,s} + \tau_f^{\mathrm{WE}(1)}$.

https://doi.org/10.1017/S0263574709990373 Published online by Cambridge University Press

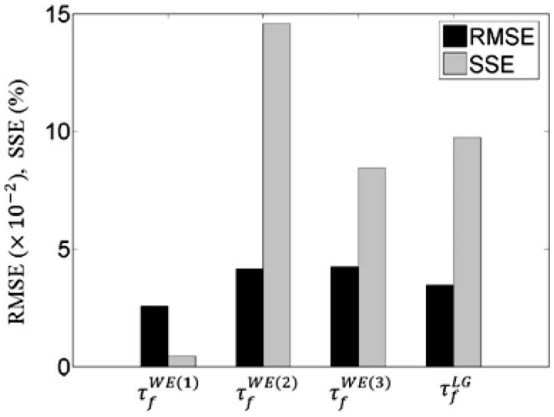



Fig. 12. Comparison values of error norms the RMSE and SSE for different friction-compensating torques for the composite controller for an SRLFJ experimental set-up.

which was obtained based on the LuGre model explained in Section 3.1. The simulation and experimental results are shown in Fig. 10 for friction torques based on the work-energy principle and the LuGre friction torque for the desired trajectory $q_d^{(1)}$. The results for other desired trajectories, $q_d^{(2)}$, $q_d^{(3)}$ and $q_d^{(4)}$, are shown later in this section.

As shown in Fig. 10(a) by using the friction-compensating torque $\tau_f^{\mathrm{LG}}$ whose design was based on the LuGre model, the error was significant; especially there was a considerable steady-state error at the end of trajectory. This error occurred since in reality the frictions at the beginning and at the end of the motion were different due to hysteresis[30] (see Fig. 6), while friction-compensating torque $\tau_f^{\mathrm{LG}}$ did not include the hysteresis effect and was the same for the beginning and end of the motion of the manipulator (see the corresponding torque in Fig. 11(a)). There was also a significant error between desired trajectory and link rotation when friction torques $\tau_f^{\mathrm{WE}(2)}$ and $\tau_f^{\mathrm{WE}(3)}$, Eqs. (84) and (85), were used. In fact, by feeding less energy into the system, using $\tau_f^{\mathrm{WE}(2)}$, the manipulator moved behind the desired trajectory, and the error remained as a negative value at the end of the motion of the robot manipulator. In contrast, by using $\tau_f^{\mathrm{WE}(3)}$, the input energy into system was more than the required energy to overcome the friction and viscous damping of the system combined. Consequently, the link moved beyond the desired trajectory, and the error became a positive value at the end of the motion. The experimental results for torques $\tau_f^{\mathrm{WE}(2)}$ and $\tau_f^{\mathrm{WE}(3)}$ are not shown here for brevity. The tracking error for $\tau_f^{\mathrm{WE}(1)}$ is shown in Fig. 10(b), where the tracking error at the end of the manipulator manoeuvre was approximately zero; and during the manipulator motion this error remained in an acceptable range. The corresponding applied torque is shown in Fig. 11(b).

Furthermore, according to the simulation results in Fig. 10, the tracking error was almost zero for both cases, the LuGre model and the WE model. That indicates that the friction-compensating torque was able to compensate for the joint friction almost completely, and the theoretical model developed for flexible-joint manipulator with joint-

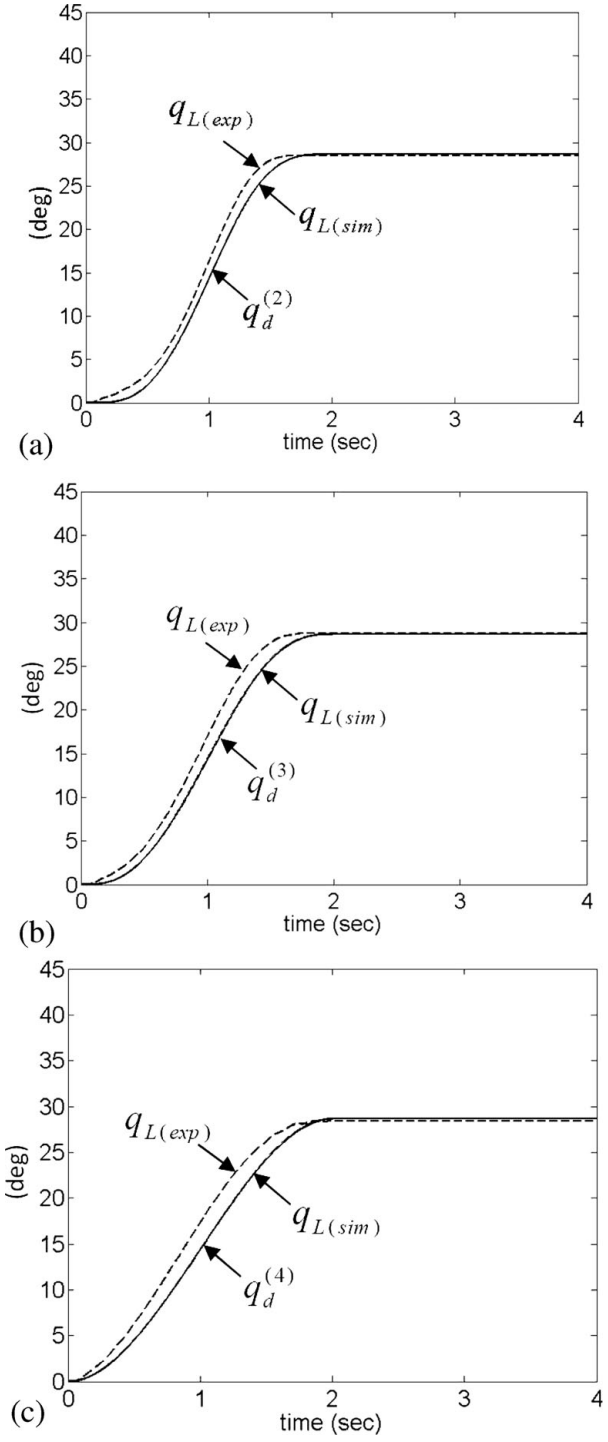



Fig. 13. Comparing simulation and experimental results of the flexible-joint manipulator manoeuvre using composite controller with link angle $q_L$ for (a) desired trajectory $q_d^{(2)}$, (b) desired trajectory $q_d^{(3)}$, (c) desired trajectory $q_d^{(4)}$.

friction given in Eqs. (32) and (33) was accurate. In the experimentation, however, there were other factors which were not possible to model them exactly (such as the effect of position and load on the friction), and consequently, there were error in the friction compensation in the experiments. To have a better assessment of the results, the root mean square error (RMSE) and steady-state error (SSE) are defined,

https://doi.org/10.1017/S0263574709990373 Published online by Cambridge University Press

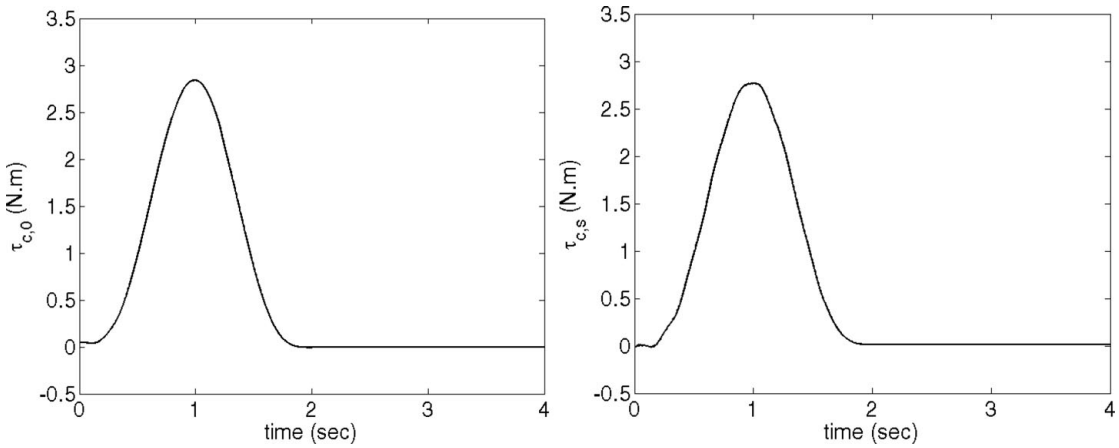



Fig. 14. (a) Rigid controller torque, $\tau_{c,0}$, based on the assumption of rigid joint; (b) composite controller torque $\tau_{c,s}$ for an SRLFJ.

Table I. Values of error norm the RMSE and SSE for different friction-compensating torques for the composite controller for an SRLFJ experimental set-up.

| Friction-compensating torque (N m) | RMSE ($\times 10^{-2}$) | SSE (%) |
|---|---|---|
| $\tau_f^{\mathrm{WE}(1)}$ (Eq. (83)) | 2.55 | 0.428 |
| $\tau_f^{\mathrm{WE}(2)}$ (Eq. (84)) | 4.16 | 14.6 |
| $\tau_f^{\mathrm{WE}(3)}$ (Eq. (85)) | 4.25 | 8.43 |
| $\tau_f^{\mathrm{LG}}$ (Eq. (86)) | 3.44 | 9.72 |

respectively, as

$$\mathrm{RMSE} = \left( \frac{1}{t_f} \int_0^{t_f} e^2 \cdot \mathrm{d}t \right)^{1/2}, \tag{87}$$

$$\mathrm{SSE} = \left| \frac{e(t_f)}{\theta_f} \right| \times 100, \tag{88}$$

where $e = q_L - q_d^{(1)}$. The RMSE shows the error between the link angle and the desired trajectory during the motion of the robot manipulator, and the SSE represents the steady-state error at the end of the manipulator manoeuvre. A summary of the results in terms of the RMSE and values of SSE are illustrated in Table I for different friction-compensating torques, and the results are then compared in Fig. 12. It can be observed that the RMSE and SSE for $\tau_f^{\mathrm{WE}(1)}$ have the minimum value of the RMSE and SSE, and it can be chosen as the best candidate.

To verify that the designed friction-compensating torque, $\tau_f^{\mathrm{WE}(1)}$, acted accurately at different trajectories, the performance of $\tau_f^{\mathrm{WE}(1)}$ was examined for other desired trajectories $q_d^{(2)}$, $q_d^{(3)}$ and $q_d^{(4)}$ given in Eqs. (77)–(79). The results are compared in Fig. 13. As shown in this figure, the manipulator follows the desired trajectories accurately. Therefore, it can be concluded that the controller works with different trajectories, from the smooth ninth order to the less smooth third order.

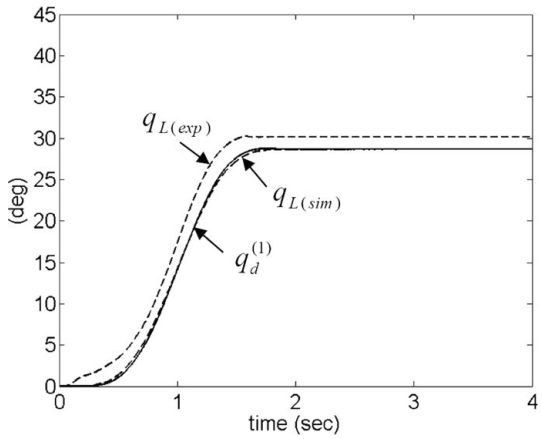



Fig. 15. Comparing simulation and experimental results of manipulator manoeuvre with rigid controller torque (link angle $q_L$ and the desired trajectory $q_d^{(1)}$) for an SRLFJ.

### 5.3. Composite controller

In this section the effectiveness of the composite controller designed for SRLFJ is studied. The results of composite controller were compared with the results of the rigid controller $\tau_{c,0}$. The rigid controller, $\tau_{c,0}$, was based on the assumption of a rigid joint and is shown in Fig. 14(a), and the composite controller $\tau_{c,s}$ is shown in Fig. 14(b). The corresponding response is compared with the desired trajectory in Fig. 15 for rigid controller. It can be seen that there is a significant tracking error between the desired trajectory and the link angle during the motion of the link ($t < t_f$) and a noticeable SSE at the end of the manipulator manoeuvre ($t > t_f$). However, by using the composite controller torque these errors were significantly reduced (see Fig. 16). For instance the value of SSE in Eq. (88) was computed as 0.026/0.50 = 5.2% when the rigid controller was used, but decreased to 0.42% when the composite controller was used. Furthermore, the value of the RMSE, which indicates the tracking error during the motion of the link, decreased from $4.10 \times 10^{-2}$ rad for the rigid controller to $2.55 \times 10^{-2}$ rad for the composite controller. In fact, the rigid controller was not able to reduce the tracking error during the manoeuvre ($t < 2$), to reach a small value before

https://doi.org/10.1017/S0263574709990373 Published online by Cambridge University Press

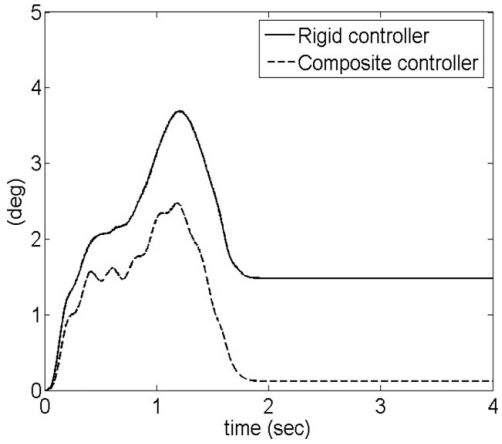



Fig. 16. Tracking error, $e = q_L - q_d^{(1)}$, between the actual link $q_L$ and the desired trajectory of the link angle $q_d^{(1)}$, for the rigid controller torque and composite controller for an SRLFJ experimental set-up.

the end of the manoeuvre ($t = 2$); the SSE remained large after ($t > 2$) because of the stiction. In contrast to the rigid controller, the composite controller had a better performance in tracking; the tracking error relatively was small during the manoeuvre, and the SSE remained small after ($t > 2$). In both approaches, the torque based on work-energy principle, $\tau_f^{\mathrm{WE}(1)}$, was employed to compensate for the friction, as this torque provided a better result compared to the LuGre torque.

## 6. Conclusion

In this study, a general control strategy for tip trajectory tracking of flexible-joint manipulators with friction was presented and experimentally validated. The first part of the controller was a linear feed-forward torque whose design was based on the work-energy principle, and it was developed to compensate for the friction in the joints. The design of the second part of the controller was based on the singular perturbation theory and the integral manifold, and it was developed to compensate for the joints' flexibility. In contrast to other controllers whose designs were based on the singular perturbation theory, the dynamic coupling between the links and actuators was considered in the dynamic modelling of the manipulators in this study. As a result, the model presented in this paper provided more accurate dynamic modelling and control of flexible-joint manipulators.

The simulation and experimental results verified the effectiveness of the designed controllers. The first part of experiments was performed to determine the efficiency of the friction-compensating strategy. Comparing this strategy with other methods such as the LuGre method confirmed the effectiveness of the proposed strategy. For instance the steady-state error, SSE, was significantly reduced from 9.72% by using the LuGre method to 0.428% by using the new proposed friction-compensating torque. Also, the accuracy of the controller was verified at different trajectories to make sure that the controller acts precisely at different velocities and accelerations.

The second part of the experiments was carried out to determine the effectiveness of the composite controller. In these experiments, it was found that the tracking error was considerably reduced during the motion of the robot arm such that the value of RMSE was decreased from $4.10 \times 10^{-2}$ rad for the rigid controller to $2.55 \times 10^{-2}$ rad for the composite controller. The maximum value of the steady-state error at the end of the manipulator was only 0.428% using the composite controller, while using the rigid controller this figure was 5.2%. Thus, using the new proposed controller would be recommended for robot manipulation tasks in which high-accuracy in trajectory tracking is desired.

## References

1. R. Fotouhi, H. Salmasi, S. Dezfulian and R. Burton, "Design and control of a hydraulic simulator for a flexible joint robot," *Adv. Rob.* **23**(6), 655–679 (2009).
2. M. W. Spong, "Control of flexible joint robots: a survey, University of Illinois," *Coordinate Science Laboratory, College of Engineering, UILU-ENG-90-2203*, University of Illinois, Urbana, IL, USA (Feb. 1990).
3. H. Diken, "Frequency-response characteristics of a single-link flexible joint manipulator and possible trajectory tracking," *J. Sound Vib.* **233**(2), 179–194 (2000).
4. B. O. Al-Bedoor and A. A. Almusallam, "Dynamics of flexible-link and flexible-joint manipulator carrying a payload with rotary inertia," *Mech. Mach. Theory* **35**(6), 785–820 (2000).
5. S. K. Spurgeon, L. Yao and X. Y. Lu, "Robust tracking via sliding mode control for elastic joint manipulators," *Proc. IMechE, Part I; J. Syst. Control Eng.* **215**(4), 405–417 (2001).
6. A. Benallegue, "Adaptive control for flexible joint robots using a passive systems approach," *Control Eng. Pract.* **3**(10), 1393–1400 (1995).
7. K. Khorasani, "Adaptive control of flexible joint robots," *Proceedings of IEEE International Conference on Robotics and Automation*, Sacramento, CA (April 1991), vol. 3, pp. 2127–2134.
8. M. Readman, *Flexible Joint Robots* (CRC Press, Boca Raton, FL, 1994).
9. M. C. Han and Y. H. Chen, "Robust control design for uncertain flexible-joint manipulators: A singular perturbation approach," *Proc. IEEE Conf. Decision Control* **1**, 611–616 (1993).
10. D. Wang, "A simple iterative learning controller for manipulators with flexible joints," *Automatica*, **31**(9), 1341–1344 (1995).
11. C. J. B. Macnab and G. M. T. D'Eleuterio, "Neuroadaptive control of elastic-joint robots using robust performance enhancement," *Robotica* **19**(6), 619–629 (2001).
12. N. Jalili, "An infinite dimensional distributed base controller for regulation of flexible robot arms," *J. Dyn. Syst. Measure. Control* **123**(4), 712–719 (2001).
13. A. Albu-Schaffer, C. Ott and G. Hirzinger, "A unified passivity-based control framework for position, torque and impedance control of flexible joint robots," *Int. J. Rob. Res.* **26**(1), 23–39 (2007).
14. M. Spong, K. Khorasani and P. Kokotovic, "An integral manifold approach to the feedback control of flexible joint robots," *IEEE J. Rob. Automat.* **3**(4), 291–300 (1987).
15. L. Sweet and M. Good, "Redefinition of the robot motion-control problem," *IEEE Control Syst. Mag.* **5**(3), 18–25 (1985).
16. H. Abdellatif and B. Heimann, "On compensation of passive joint friction in robotic manipulators: modeling, detection and identification," *IEEE International Conference on Control Applications*, Munich (Oct. 2006) pp. 2510–2515.

https://doi.org/10.1017/S0263574709990373 Published online by Cambridge University Press

17. G. Liu, A. A. Goldenberg and Y. Zhang, "Precise slow motion control of a direct-drive robot arm with velocity estimation and friction compensation," *Mechatronics* **14**(7), 821–834 (2004).
18. C. Canudas de Wit, H. Olsson, K. J. Astrom and P. Lischinsky, "A new model for control of systems with friction," *IEEE Trans. Automat. Control* **40**(3), 419–425 (1995).
19. M. K. Ciliz, "Adaptive control of robot manipulators with neural network based compensation of frictional uncertainties," *Robotica* **23**(2), 159–167 (2005).
20. P. Tomei, "Robust adaptive friction compensation for tracking control of robot manipulators," *IEEE Trans. Automat. Control* **45**(11), 2164–2169 (2000).
21. J. C. Piedboeuf, J. de Carufel and R. Harteau, "Friction and stick-slip in robots: simulation and experimentation," *Multibody Syst. Dyn.* **4**(4), 341–354 (2000).
22. M. Grotjahn, M. Daemi and B. Heimann, "Friction and rigid body identification of robot dynamics," *Int. J. Solids Struct.* **38**(10), 1889–1902 (2001).
23. B. Subudhi and A. S. Morris, "Singular perturbation based neuro-$H_\infty$ control scheme for a manipulator with flexible links and joints," *Robotica* **24**(2), 151–161 (2006).
24. F. Ghorbel and M. W. Spong, "Integral manifolds of singularly perturbed systems with application to rigid-link flexible-joint multibody systems," *Int. J. Non-Lin. Mech.* **35**(1), 133–155 (2000).
25. J. H. Ginsberg, *Advanced Engineering Dynamics*, 2nd ed. (Cambridge University Press, New York, USA, 1995).
26. P. V. Kokotovic, H. K. Khalil and J. O'Reiley, *Singular Perturbation Methods in Control: Analysis and Design* (Academic Press, New York, 1986).
27. B. Siciliano and W. J. Book, "A singular perturbation approach to control of lightweight flexible manipulators," *Int. J. Rob. Res.* **7**(4), 79–90 (1988).
28. A. Ferrara and L. Magnani, "Motion control of rigid robot manipulators via first and second order sliding modes," *J. Intell. Rob. Syst.* **48**(1), 23–36 (2007).
29. S. Torres, J. A. Mendez, L. Acosta and V. M. Becerra, "On improving the performance in robust controllers for robot manipulators with parametric disturbances," *Control Eng. Pract.* **15**(5), 557–566 (2007).
30. B. Armstrong-Hélouvry, *Control of Machines with Friction* (Kluwer Acadamic, Norwell, MA, 1991).

## Appendix A. Dynamic equations of two-rigid-link flexible-joint manipulator

Equations (29) and (30) were derived using the Euler–Lagrange method. For instance for a two-rigid-link flexible-joint manipulator, eqs. (29) and (30) were written as

$$\begin{bmatrix} D_{11} & D_{12} \\ D_{21} & D_{22} \end{bmatrix} \begin{bmatrix} \ddot{q}_{l_1} \\ \ddot{q}_{l_2} \end{bmatrix} + \begin{bmatrix} 0 & C_{l_1} \\ C_{l_2} & 0 \end{bmatrix} \begin{bmatrix} \dot{q}_{l_1} \\ \dot{q}_{l_2} \end{bmatrix} + \begin{bmatrix} k_1 & 0 \\ 0 & k_2 \end{bmatrix} \times \left( \begin{bmatrix} q_{l_1} \\ q_{l_2} \end{bmatrix} - \begin{bmatrix} q_{m_1} \\ q_{m_2} \end{bmatrix} \right) = \begin{bmatrix} H_{11} & H_{12} \\ H_{21} & H_{22} \end{bmatrix} \begin{bmatrix} \tau_1 \\ \tau_2 \end{bmatrix}, \tag{A1}$$

$$\begin{bmatrix} J_{11} & 0 \\ 0 & J_{22} \end{bmatrix} \begin{bmatrix} \ddot{q}_{l_1} \\ \ddot{q}_{l_2} \end{bmatrix} - \begin{bmatrix} k_1 & 0 \\ 0 & k_2 \end{bmatrix} \left( \begin{bmatrix} q_{l_1} \\ q_{l_2} \end{bmatrix} - \begin{bmatrix} q_{m_1} \\ q_{m_2} \end{bmatrix} \right) = \begin{bmatrix} \tau_1 \\ \tau_2 \end{bmatrix}, \tag{A2}$$

where

$$\begin{aligned}
D_{11} &= I_{l_1} + m_{l_1} l_{c_1}^2 + m_{l_2} l_1^2 + m_t l_1^2 + I_{h_2} + m_{h_2} l_1^2, \\
D_{12} &= m_{l_2} l_1 l_{c_2} \cos(q_{l_2} - q_{l_1}) + m_t l_1 l_2 \cos(q_{l_2} - q_{l_1}), \\
D_{21} &= D_{12}, \\
D_{22} &= I_{l_2} + m_{l_2} l_{c_2}^2 + I_t + m_t l_2^2, \\
C_{l_1} &= -(m_{l_2} l_1 l_{c_2} + m_t l_1 l_2) \sin(q_{l_2} - q_{l_1}) \dot{q}_{l_2}, \\
C_{l_2} &= (m_{l_2} l_1 l_{c_2} + m_t l_1 l_2) \sin(q_{l_2} - q_{l_1}) \dot{q}_{l_1}, \\
J_{11} &= I_{r_1}, \\
J_{22} &= I_{r_2}, \\
H_{11} &= 0, \\
H_{12} &= -1, \\
H_{21} &= 0, \\
H_{22} &= 0.
\end{aligned}$$

For $i = 1, 2$, parameter $\tau_i$ was the applied torque to joint $i$; $m_{l_i}$ was the mass of link $i$; $m_t$ was the mass of the manipulator's tip; $l_i$ was the length of link $i$; $l_{c_i}$ was the distance of the centre of mass of link $i$ from joint $i$ axis. Parameters $I_{l_i}$, $I_t$, $I_{h_i}$ and $I_{r_i}$ were respectively mass moments

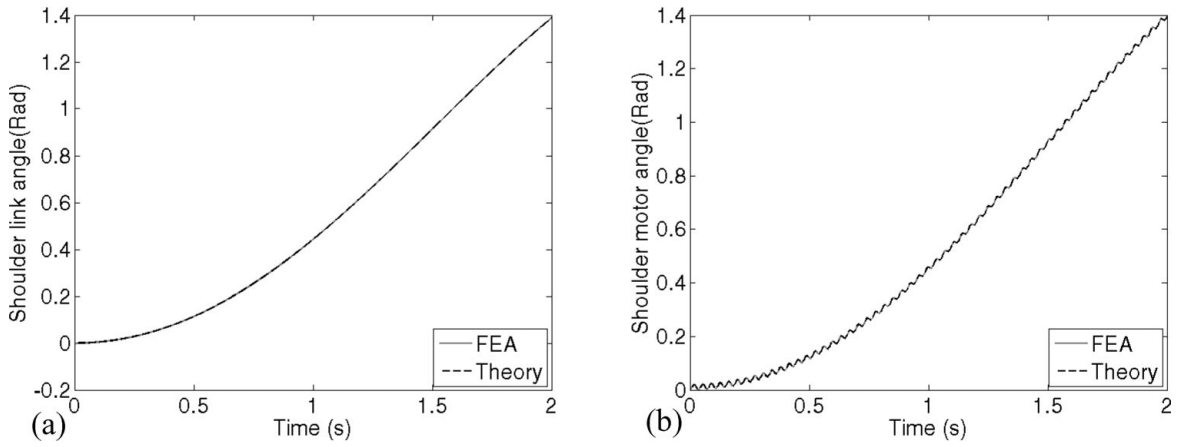



Fig. 17. Comparison results of FEA and theoretical method for a two-rigid-link flexible-joint manipulator: (a) shoulder link rotation and (b) shoulder joint rotation.

https://doi.org/10.1017/S0263574709990373 Published online by Cambridge University Press

of inertia of link $i$, manipulator's tip, hub of joint $i$ and rotor of joint $i$. Also, in Eqs. (A1) and (A2) rotations of links $q_{l_i}$ and rotations of joints $q_{m_i}$ were measured in the absolute coordinate frames. The frame of the first link (shoulder link) was a Cartesian coordinate fixed to the first joint (shoulder joint). The frame of the second link (elbow link) was also a Cartesian coordinate system fixed to the second joint (elbow joint) and was parallel to the shoulder frame during the motion.

The numerical values used for verification were $\tau_1 = 0.3$ N m, $\tau_2 = 0.1$ N m, $l_1 = l_2 = 0.5$ m, $l_{c_1} = l_{c_2} = 0.25$ m, $I_{r_1} = I_{r_2} = 1 \times 10^{-3}$ kg m$^2$, $I_{h_1} = I_{h_2} = 3 \times 10^{-4}$ kg m$^2$, $I_t = 1 \times 10^{-3}$ kg m$^2$, $k_1 = k_2 = 30$ N m/rad, $m_{l_1} = m_{l_2} = 0.39$ kg, $I_{l_1} = I_{l_2} = 8.1 \times 10^{-3}$ kg m$^2$, $m_t = 0.2$ kg, $m_{h_1} = m_{h_2} = 0.2$ kg. The correctness of dynamic equations of (A1) and (A2) were validated using FEA. The results for rotations of shoulder link and shoulder joint are compared in Fig. 17. According to this figure, the results of FEA and theoretical approach confirm each other.

## Appendix B. Deriving the dynamic equations of the flexible-joint manipulator for $\mu = 0$

Equation (48) can be written as

$$\begin{aligned}
\ddot{x} &= -D^{-1}C_l\dot{x} + D^{-1}[D(J+D)^{-1}J][D^{-1}C_l\dot{x} \\
&\quad + (J^{-1} - D^{-1}H)\tau_c] + D^{-1}H\tau_c \\
&= [-D^{-1} + (J+D)^{-1}JD^{-1}]C_l\dot{x} - (J+D)^{-1}\tau_c \\
&\quad - D^{-1}[J(J+D)^{-1}D]D^{-1}H\tau_c + D^{-1}H\tau_c \\
&= -(J+D)^{-1}[(J+D)D^{-1} - JD^{-1}]C_l\dot{x} \\
&\quad + (J+D)^{-1}\tau_c - D^{-1}J(J+D)^{-1}H\tau_c + D^{-1}H\tau_c \\
&= -(J+D)^{-1}C_l\dot{x} + (J+D)^{-1}\tau_c + [-D^{-1}J \\
&\quad + D^{-1}(J+D)](J+D)^{-1}H\tau_c \\
&= -(J+D)^{-1}C_l\dot{x} + (J+D)^{-1}\tau_c + (J+D)^{-1}H\tau_c \\
&= (J+D)^{-1}[-C_l\dot{x} + (H+I)\tau_c].
\end{aligned}$$

https://doi.org/10.1017/S0263574709990373 Published online by Cambridge University Press